ACS APPLIED MATERIALS & INTERFACES

Research Article

www.acsami.org

Supersonically Blown Ultrathin Thorny Devil Nanofibers for Efficient Air Cooling

Seongpil An,[†] Changmin Lee,[†,‡] Minho Liou,[†] Hong Seok Jo,[†] Jung-Jae Park,[†] Alexander L. Yarin,*[,§,∥] and Sam S. Yoon*[,†]

[†]School of Mechanical Engineering, [‡]Green School, and [§]College of Engineering, Korea University, Seoul 136-713, Republic of Korea
[∥]Department of Mechanical and Industrial Engineering, University of Illinois at Chicago, Illinois 60607-7022, United States

ABSTRACT: The effect of the supersonically blown below-74 nm nanofibers on cooling of high-temperature surfaces is studied experimentally and theoretically. The ultrathin supersonically blown nanofibers were deposited and then copper-plated, while their surfaces resembled those of the thorny-devil nanofibers. Here, we study for the first time the enhancement of surface cooling in gas in the cases of the forced and natural convection with the help of ultrathin thorny-devil nanofibers. These polymer core−metal shell nanofibers in nanometric scale possess a relatively high thickness of the metal shell and a high effective thermal conductivity, which facilitates heat transfer. The additional surface temperature reduction close to 5 °C in the case of the forced convection in the impinging air jet and close to 17 °C in the case of the natural convection was achieved. Correspondingly, an increase in the value of the heat transfer coefficient of about 41% in the forced convection, and about 20% in the natural convection was achieved due to the presence of the thorny devil electrospun and/or supersonically blown nanofibers.

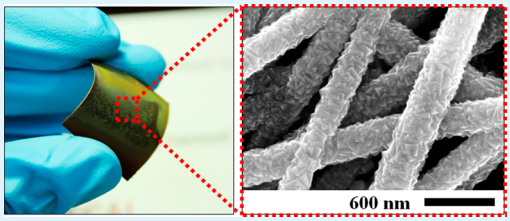

KEYWORDS: *electrospinning, nanofibers, electroplating, supersonic nanoblowing, heat removal, cooling microelectronics*

1. INTRODUCTION

While a recent technological trend requires miniaturization of electronic devices, it causes an increase in the heat release rate per unit volume, which poses serious problems in spite of the fact that the surface-to-volume ratio increases. Heat sinks and fans have been widely used to remove heat from electronic devices; however, their application is limited by narrow material choices.[1−4] There are some other means of microelectronics cooling. For example, laptops use a fan installed inside while taking advantage of the convective heat transfer or wind/air chill. However, a large server room (such as Google server rooms) experiences an enormous heat release, and thus, air cooling alone is insufficient. Thus, water cooling is proposed and tested. In case of unmanned aerial vehicles (UAVs) or commercial and military jets, complex electronics and equipment [such as electro-optical infrared sensors, video equipment, signal-processing systems, real-time image processing, heating, ventilation, and air conditioning (HAVC) systems, etc.] inside need to be cooled continually to avoid any overheating that eventually leads to malfunction or failure.[5−7] The line replacement unit (LRU) used in such cases consists of multiple fans that enhance convective cooling. However, the convective cooling is limited by small space available and other technological limitations, as well as high cost. For these reasons, spray cooling is considered as a realistic option, and nanotextured surfaces were developed to enhance it.[8] In the latter work and subsequent works, electroplating of electrospun polyacrylonitrile (PAN) nanofiber mats with copper resulted in the so-called "thorny devil" nanofibers with fractal-like surfaces and dramatically increased surface area of individual nanofibers.[8−11] Polymer nanofiber mats (without metal-plating) significantly enhance heat removal in drop cooling because they eliminate receding motion and bouncing of spread-out drops and thus dramatically enhance coolant contact with the surface.[12] Even at such high surface temperatures as 300 °C, water and ethanol drops cannot leave the hot surface, as in the anti-Leidenfrost effect discovered in refs 13 and 14.

It should be emphasized that cooling enhancement by means of the thorny devil nanofibers was demonstrated so far only in liquid cooling. Herein, we show, for the first time, that air cooling can also be significantly enhanced by means of nanotextured surfaces covered by thorny devil copper-plated 40−100 nm nanofibers formed by the novel process of supersonic blowing applied in the present work to PAN. The solution blowing of nanofibers from polymer solution jets at subsonic gas speed was introduced in refs 15−17 and was recently extended to the case of much higher supersonic speeds of the blowing gas.[18] Transition to supersonic speeds of blowing is achieved using a converging-diverging Laval nozzle, which is the approach originating from gasdynamics and the large-scale aerospace applications.[19−21] Supersonic blowing of graphene powder demonstrated recently[22] also employs the Laval nozzles. In the present work, we use the electrically assisted solution blowing to form below-74 nm PAN nanofibers to facilitate cooling of hot surfaces.

Received: May 21, 2014
Accepted: July 13, 2014
Published: July 14, 2014

 © 2014 American Chemical Society

2. EXPERIMENTAL SECTION

2.1. Precursors. Polyacrylonitrile (PAN) and dimethylformamide (DMF) were purchased from Sigma-Aldrich (Seoul, Korea) and Reagents Duksan (Ansan, Korea), respectively. The materials for copper electroplating, copper sulfate, hydrochloric acid, and formaldehyde were obtained from Sigma-Aldrich, and sulfuric acid was obtained from Matsunoen Chemicals (Osaka, Japan). To form PAN nanofibers, 6 wt % of PAN was dissolved in DMF, while stirring by magnetic stirrer for 24 h at room temperature. As for the electroplating solution, sulfuric acid (10 g), hydrochloric acid (1 g), copper sulfate (32 g), and formaldehyde (20 g) were mixed with 200 mL of deionized (DI) water. Sulfuric acid increased solution conductivity for enhancement of the electroplating process.[8]

2.2. Nanofibers. The PAN 6 wt % solution was supplied by a syringe pump (KDS LEGATO 100) at the flow rate of $Q = 150\ \mu L/h$ to a needle [with the inner and outer diameters being 0.25 and 0.52 mm, respectively (EFD 25 gauge)] attached to a dc source (Glassman High Voltage Inc., EL40P1). The applied voltage was in the range 5−6 kV. The nozzle-to-substrate distance was 10 cm. The needle was located at 3 cm downstream from the nozzle exit and 2 cm above the centerline of the nozzle (Figure 1). A grounded Laval nozzle was used

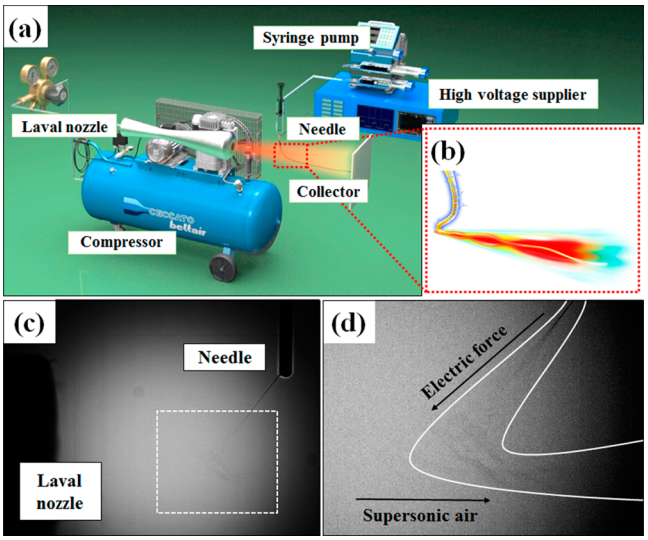

Figure 1. Supersonic nanoblowing setup. (a) Overall view. (b) Polymer jet bending and stretching in the supersonic air jet. (c and d) Images of the initial section of the electrified polymer jet issued from the needle and attracted to the grounded Laval nozzle captured by a CCD (Vision Research Inc., Phantom 9.1, at the frame rate of ∼2000 fps). Panel c shows the overall view, and panel d shows the zoomed-in view corresponding to the dashed square in panel c. Even at ∼2000 fps, it was practically impossible to resolve in detail the bending instability of the polymer jet, as accurate as it was done in refs 42 and 44.

for solution blowing as described in the following subsection. The polymer jet issued from the needle under the action of the electric force and attracted to the grounded Laval nozzle was swiped in its vicinity by the supersonic air jet issued from the Laval nozzle. A flexible thin copper plate was used as a grounded substrate because it was the most appropriate for the subsequent electroplating procedure described below. Other metal or nonmetal plates (i.e., aluminum foil, ITO glass, etc.) could also be used as substrates. However, they do not result in a desirable thorny-devil structure of electroplated PAN nanofibers.

2.3. Supersonic Blowing. A Laval converging-diverging supersonic nozzle was used to issue a supersonic air jet, which entrained polymer jet attracted electrically to it. The Laval nozzle had the following dimensions: 4.0, 3.5, and 4.5 mm for inlet, throat, and outlet diameters, respectively. The lengths of the converging and diverging sections of the Laval nozzle were 40 mm and 90 mm, respectively. Air was delivered to the nozzle entrance at 30 °C (in the nonpreheated case) and 500 °C in the case with preheating). In both cases, supersonic air jets were issued from the nozzle. However, in the case with preheating, a much higher air velocity (exceeding ∼900 m/s) at the Laval nozzle exit was achieved. On the other hand, in the nonpreheated case the maximum velocity of about ∼470 m/s was achieved. For preheating, a gas heater (Joowon H&C, Seoul, Korea) was used. It should be emphasized that, even in the case of preheating, air jet at the Laval nozzle exit had already transferred so much of its internal thermal energy into its kinetic energy that its temperature was low enough (less than ∼200 °C) to prevent thermal degradation of the polymer jet, which stayed spinnable. We also measured the static gas temperature at $z = 10$ cm downstream from the nozzle exit and $r = 10$ cm radially away from the centerline for both the $T_o = 30$ °C (nonpreheated) and 500 °C (preheated) cases, where T_o is the stagnation or chamber gas temperature. The measured surrounding static temperature was $T_\infty = 30$ and 100 °C. The reason why the original temperature was not recovered for the preheated case (T_o = 500 °C) was that the preheated jet cooled due to the heat losses.

The supersonic air jet applied an additional significant aerodynamic stretching (directly and through the aerodynamically driven bending instability) to the polymer jet attracted to it by the electric forces. Thus, polymer nanofibers were formed. They were practically dried in flight due to rapid solvent evaporation and deposited at a substrate located at a distance of 20 cm downstream from the Laval nozzle exit.

Figure 1 shows the supersonic nanoblowing setup, which included the Laval nozzle and compressor. The compressor provides the high pressured air, which is heated and expanded through the nozzle. The syringe pump feeds the polymeric solution, which is charged by the high voltage supplier. The electrospun nanofiber is ejected through the needle and entrained into the supersonic air stream. The supersonically blown nanofibers are collected onto a substrate.

2.4. Electroplating. The nanofibers were gold-sputtered to make them slightly conductive, so that electroplating can be conducted. Then, the sputtered nanofibers were immersed into the copper electroplating solution on a cathode, which was in contact with a −3 V voltage source compared to the anode. The electric current density of 100 mA/cm^2 was sustained in the bath for 1 min (the electroplating duration). As in ref 8, a pure copper plate was used as an anode, where the copper ions Cu^{2+} and Cu^{+} were released following the reactions[23,24] $Cu \rightarrow 2e^- + Cu^{2+}$ or $Cu \rightarrow e^- + Cu^{+}$. These ions were attracted to the nanofiber mat on the cathode, where copper-plating took place following the reactions $Cu^{2+} + 2e^- \rightarrow Cu$ or $Cu^{+} + e^- \rightarrow Cu$. Finally, the electroplated nanofibers were rinsed in DI water for a few seconds. The rinsed copper-plated nanofiber mats were dried in open air for 24 h.

2.5. Characterization. Polymer and copper-plated nanofibers were characterized using a high resolution scanning electron microscope (SEM, Hitachi S-5000). The size distribution of the nanofibers was evaluated by direct measurement of about ∼200 nanofibers taken from the SEM images. To observe the growth pattern and thickness of the electroplated copper layer on PAN nanofibers, we used a high-resolution transmission electron microscopy [HR-TEM, JEOL field-emission TEM (2100F) operated at 200 kV].

3. RESULTS AND DISCUSSION

3.1. Supersonic Solution-Blown Nanofibers. Panels c and d of Figure 1 show images of the electrified polymer solution jet issued from a needle and attracted to the grounded Laval nozzle. The polymer jet is swiped by the supersonic air jet issued from the Laval nozzle. On its way from the needle to the Laval nozzle, polymer jet experiences the electrically driven bending instability. After the polymer jet is swiped by the supersonic air jet, the former experiences a very strong aerodynamically driven stretching and bending.[18]

Figure 2 depicts the computational results of the supersonic air jet corresponding to our Laval nozzle and operating

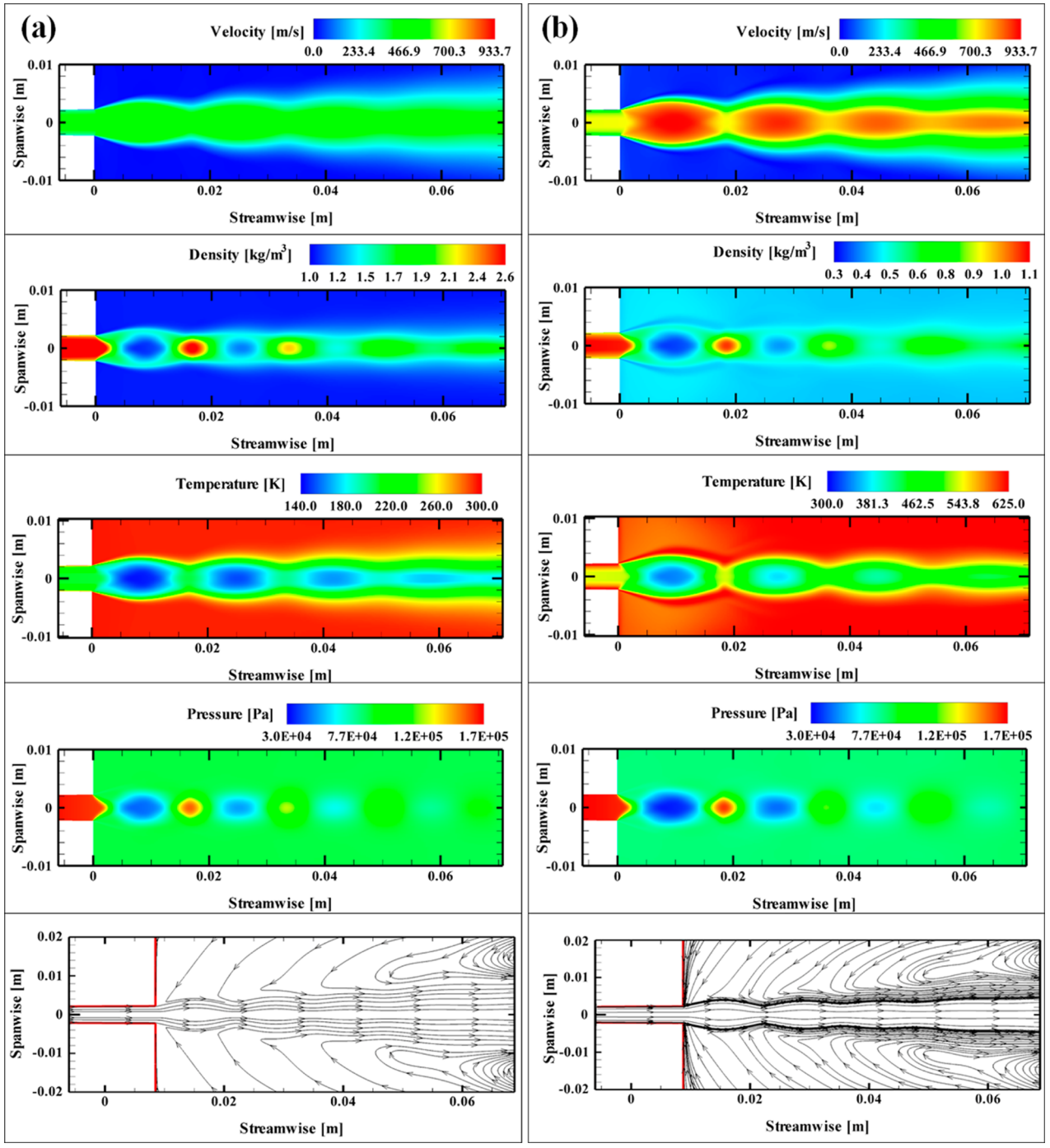

Figure 2. Longitudinal velocity, density, temperature, and pressure fields, as well as the streamlines at (a) 30 °C and (b) 500 °C air temperature at the entrance to the Laval nozzle.

conditions. The results were obtained using Fluent 6.3 (Fluent Inc., 2008), which solves the full Navier–Stokes equations of a compressible flow. Even though viscous effects and turbulence are included in the calculations, the obtained air flow pattern is dominated by purely gasdynamical (compressibility) effects. Indeed, the flow structures obtained in our 2D calculations (using the second-order accurate numerical approximation for the derivatives in the Navier–Stokes equations) depicted in Figure 2 reveal a system of several normal shocks outside the nozzle. Such flow structures are characteristic of the outflows from Laval nozzles in cases where the outside pressure is lower than the one corresponding to a smooth ideal outflow predicted by the 1D theory of Laval nozzles.[19] The flow at the exit of the Laval nozzle was slightly under-expanded (P_{exit} = 1.7 atm > P_{amb} = 1.0 atm), which always causes the formation of a system of detached shock waves outside.[19]

In Figure 2 the computational domain outside the nozzle extends 400 mm downstream, beyond which the system of the shocks was fully dissipated by viscous losses. The stagnation pressure at the nozzle inlet was P_0 = 6 bar, while the stagnation temperatures were either T_0 = 30 °C (no preheating) or 500 °C (preheating). It should be emphasized that the main purpose of the gas preheating is to convert more thermal energy into kinetic energy using the Laval nozzle, that is, to increase the gas

velocity. When such conversion happens, the temperature drastically diminishes, see Figure 2, where the gas temperature at the nozzle exit (where the polymer solution jet comes in contact with the gas flow) is much lower than 500 °C. This higher blowing velocity triggers the faster evaporation of polymer solution jet affected by the gas jet, which is reflected in the size and surface morphology of the blown nanofibers (see Figures 3 and 4). More detailed descriptions of the computational approach were provided in our previous publications.[25,26]

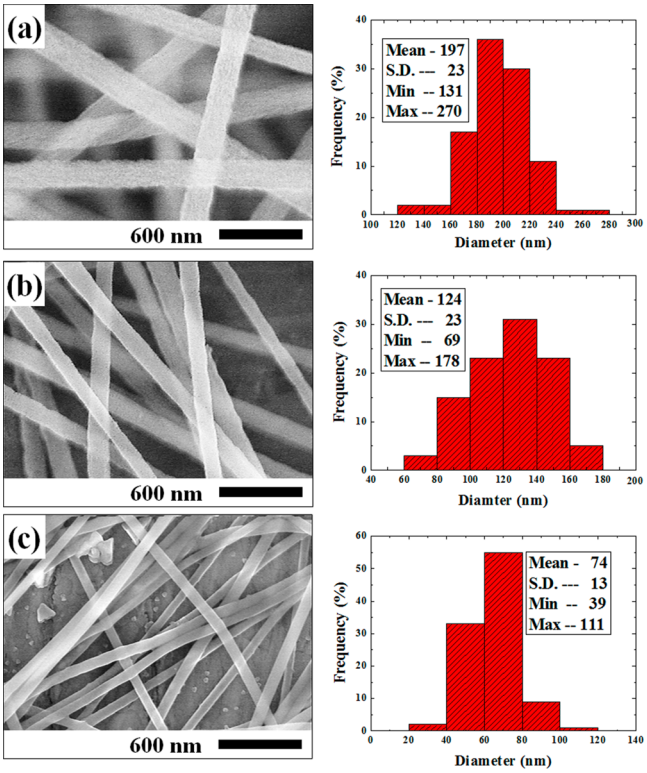

Figure 3. SEM images of PAN nanofibers and the corresponding fiber distributions. (a) After pure electrospinning without supersonic blowing. (b) After the electrically assisted supersonic blowing without preheating. (c) After the electrically assisted supersonic blowing with preheating.

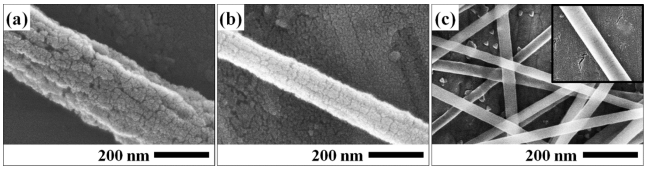

Figure 4. High magnification SEM images. (a) Purely electrospun nanofiber without supersonic blowing. (b) Nanofiber formed by the electrically assisted supersonic blowing without preheating. (c) Nanofibers formed by the electrically assisted supersonic blowing with preheating. Compare the surface nanotexture of the individual nanofibers seen before copper-plating (in the present images) with the nanotexture seen in Figure 6 after copper-plating.

Figure 2 shows that the flow accelerates in the diverging section of the Laval nozzle and become supersonic. As expected, the preheating results in a significantly higher outflow velocity than the one without preheating, albeit in both cases (with and without preheating) supersonic outflow regimes were achieved (~933 m/s and ~470 m/s, respectively). In the calculations, the air density was initially set to 1.23 kg/m^3 in all cases. For the 30 °C case (Figure 2a), the density of air surrounding the supersonic jet outside the nozzle was about ~1.0 kg/m^3; that is, it is slightly lower than the one before the nozzle inlet. Viscous forces result in the entrainment of the surrounding air into the jet issued from the Laval nozzle as the streamlines in Figure 2 show. Figure 2 also shows that at the nozzle exit the supersonic air jets are subcooled due to transfer of their internal energy into the kinetic one inside the Laval nozzle. The temperature of the air jet increases stepwise after each compression in the normal shocks.

Note also that stretching by supersonic gas jet overbears any potential change in the polymer solution temperature and increase in viscosity. Indeed, the characteristic cooling time of a section of the polymer jet when it begins to interact with the gas jet is $\tau_{cooling} \sim d^2/\alpha$, and the characteristic stretching time in this element is $\tau_{stretching} \sim d/C$, where d is the cross-sectional radius, α is the thermal diffusivity of solution, and C is the speed of sound in gas. The estimates yield $\tau_{cooling} \sim 10^{-5}$ s, and $\tau_{stretching} \sim 10^{-11}$ s, which means that the jet element will be stretched much faster than its bulk temperature (and thus the viscosity) will change.

Figure 3a shows the SEM image and the corresponding fiber-size distribution of PAN nanofibers formed by pure electrospinning without supersonic blowing. The cross-sectional nanofiber diameter is in the range 160−240 nm, and the mean diameter is about 197 nm. Figure 3b shows the SEM image and the corresponding fiber-size distribution of PAN nanofibers formed by the electrically assisted solution blowing without preheating with the inlet air temperature being 30 °C. It is seen that due to the blowing the nanofiber mean diameter was reduced to about 124 nm. Figure 3c shows the SEM image and the corresponding fiber-size distribution of PAN nanofibers formed by the electrically assisted solution blowing with preheating with the inlet air temperature being 500 °C. In this case, the nanofiber diameter is in the range of 40−100 nm and the mean diameter is about 74 nm, which is the finest PAN nanofibers reported in literature, as to our knowledge. According to ref 18, supersonic blowing causes a substantial stretching rate of nanofibers. That allows one to expect that the supersonically blown nanofibers will be thinner than the electrospun one, and the thinning will be stronger at higher air flow speeds (under preheating), which is fully confirmed by the results in Figure 3.

Figure 4 shows that nanofiber morphology varies depending on the forming conditions. It is seen that the surface texture of the fibers becomes smoother when their diameter decreases. The diameter decrease significantly increases the surface area to volume ratio, which makes the solvent evaporation process faster and more uniform. This is probably facilitated by a higher surrounding temperature, as Figure 4**c** reveals. It should be emphasized that the surface texture or roughness of the nanofibers in Figure 4c could not be resolved at the magnification used. It is also noteworthy that the supersonic blowing at 30 and 500 °C did not cause any thermal degradation or phase change of the PAN nanofibers, based on the FTIR results (not shown here).

3.2. Copper-Electroplated Nanofibers. Figure 5 shows a copper-foil substrate at different stages of nanofiber deposition, gold-sputtering, and copper-plating. It also demonstrates flexibility of the substrate with the deposited copper-plated nanofiber mat.

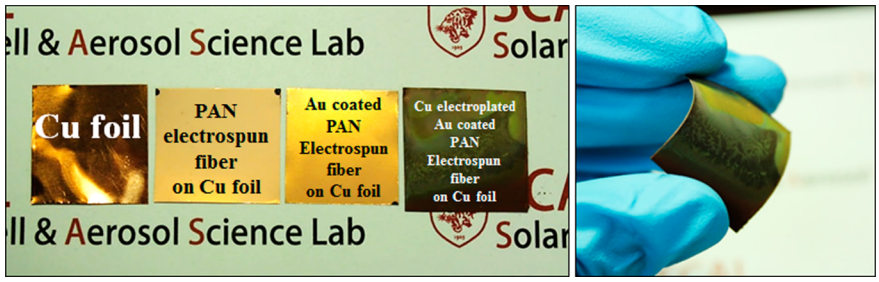

Figure 5. Copper-plated supersonically blown PAN nanofibers on a flexible substrate (Cu foil). From the left: The substrate-Cu foil, polymer PAN solution-blown nanofibers deposited onto the substrate, the nanofibers on the substrate after gold-sputtering, the nanofibers on the substrate after gold-sputtering and a subsequent copper-plating. The substrate flexibility is shown on the utmost right.

Figure 6 shows SEM images and the corresponding fiber-size distributions of copper-plated nanofibers. The fiber morphology resembles the one of the so-called thorny devil nanofibers.[8] Such morphologies are controlled by choosing the conditions of the electroplating process, which affects the nucleation rate and the crystal growth rate. The surface morphologies seen in Figure 6 are nanotextured, fractal-like, and sharp. Such surface structures dramatically increase the total surface area of individual nanofibers and thus are attractive having in mind enhancement of heat transfer. Similar electroplating conditions were used for all cases shown in Figure 6. However, the difference in the mean diameters in the two cases (purely electrospun and solution-blown without preheating) is insignificant; they are close to about 270 nm. On the other hand, the mean diameter in the third case (solution-blown with preheating) is still significantly smaller-about 164 nm.

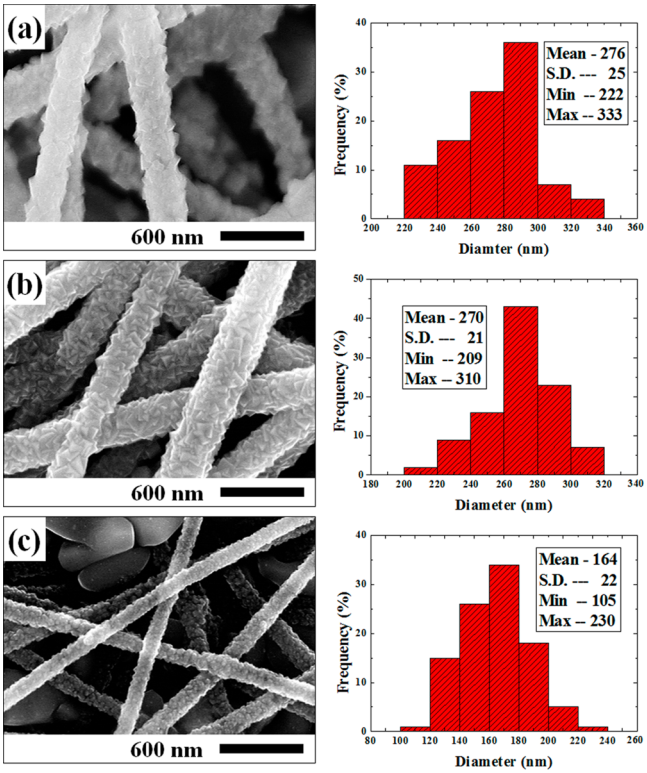

Figure 6. SEM images of copper-plated nanofibers. (a) After pure electrospinning without supersonic blowing. (b) After the electrically assisted supersonic blowing without preheating. (c) After the electrically assisted supersonic blowing with preheating.

Comparing the mean diameters of the copper-plated nanofibers in Figure 6a, b, and c (276, 270, and 164 nm, respectively) with the corresponding ones in Figure 3a, b, and c before copper-plating (197, 124, and 74 nm, respectively), one can see that the electroplating process increased the nanofiber diameters by the factors of 1.4, 2.18, and 2.22, respectively. It is clear that smaller nanofiber diameters, and thus their higher curvatures, facilitate concentration of the electric field lines in the electroplating bath and thus facilitate deposition of copper ions (indeed, the electric field strength near a cylindrical electrode-a nanofiber-is inversely proportional to its cross-sectional radius). This indicates that the relative mass of copper in the nanofiber shells as compared to that of PAN in their cores is higher in the solution-blown nanofibers, which is an additional benefit for heat transfer enhancement. Indeed, the polymer core−metal shell structures in nanometric scale with a high relative thickness of the metal shell possess a high effective thermal conductivity, which facilitates heat transfer.

Figure 6c also shows a larger interfiber porosity in the case of the supersonically blown nanofibers formed with air preheating at the inlet of the Laval nozzle to 500 °C, as compared to the other two cases in Figure 6. This stems from the fact that a higher air velocity in the impinging jet definitely results in a wider fiber deposition onto a substrate in the lateral direction.

The thorny devil nanofibers could be detached from the copper foil or any other substrate by scratching. These detached nanofibers were randomly placed on a TEM sampling container and their TEM images were obtained. Figure 7 shows TEM image of a copper-plated thorny devil nanofiber, which was formed by the electrically assisted supersonic blowing with air preheating at the inlet of the Laval nozzle to 500 °C. It is seen that, in this case, the core PAN nanofiber diameter is

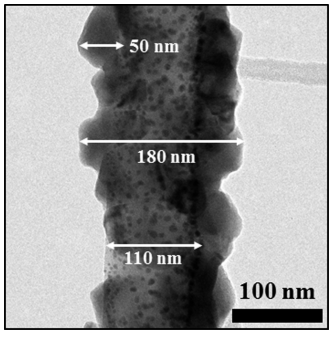

Figure 7. TEM image of a copper-plated thorny devil nanofiber, which was supersonically- blown with air preheating at the inlet of the Laval nozzle up to 500 °C.

dx.doi.org/10.1021/am503139n | ACS Appl. Mater. Interfaces 2014, 6, 13657−13666

about ~110 nm and the copper-plated shell extends it up to about ~180 nm, and thus, the copper layer (the outer shell) has a thickness of less than ~70 nm. Thus, the shell/core diameter ratio is about 1.64, which is smaller than the mean value of 2.22 reported above. The dots visible in Figure 7 are the Au residues from sputtering, which precede copper-plating.

3.3. Turbulence Effect. To assess the effect of the thorny devil nanofibers on heat removal rate in air cooling, nanofiber-coated substrate (or mat of A = 3 cm × 3 cm in size) was located on a heater (or plate) placed on an aluminum block. The steady state temperature of 120 °C of the bare copper substrate was maintained by a constant power supply to the heater plate. The total power supplied to the heater was $Q_t = IV$ = (0.275 Amp) × (150 V) = 41.25 W (with I being the electric current and V being voltage). It was divided into all planes of the rectangular heater and the aluminum block whose total surface area was about A_t = 380 cm^2 while the substrate surface occupied only A = 9 cm^2. As a result, the amount of heat released through the substrate surface was roughly $Q = (A/A_t)$ Q_t = (9/380) (41.25 W) ~ 0.977 W.

Alternatively, using for the estimate the correlation of section 7-6 in ref 27 for the natural convection heat removal from a horizontal plate in steady state, the heat supplied to the top plate alone was estimated to be about Q ~ 0.93 W, which is consistent with the value of Q = 0.977 W listed above. As a result, the heat flux at the top plate where the nanofiber mat was located was estimated to be about $q = Q/A$ = 1.03 kW/m^2, where A = 9 cm^2 and Q = 0.93 W, which was considered to be the heat supplied to the top plate alone.

A thermocouple (MV1000, Yokogawa, Japan) was placed between the hot plate and the nanofiber mat to record the effect of cooling. Air at room temperature (about 19 °C) was blown by a fan located above the mat, as depicted in Figure 8. This is the forced-convection cooling case. Conversely, the experiment without fan blowing corresponded to the natural convection case and was the buoyancy dominated.

We studied three major cases: (i) The mat was coated with electrospun (ES) nanofibers, (ii) electrospun nanofibers subsequently electroplated (ES + EP), or (iii) supersonic-blown electrospun nanofibers subsequently electroplated (SES + EP). Certainly, the electroplated cases would result in better cooling than the case without electroplating because electroplating introduces copper thorns on nanofibers of high roughness and thermal conductivity which facilitates enhanced heat transfer.

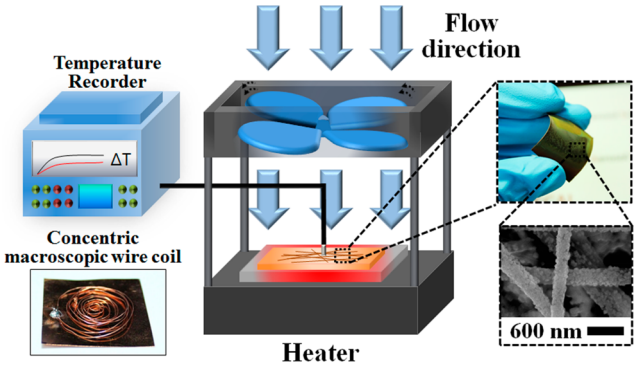

Figure 8. Schematic of the air cooling experimental setup. The air-blowing fan (5 cm diameter, 3800 rpm) is located at 2.5 cm above the heated nanofiber mat (3 cm × 3 cm). The fan produced a cold air jet impinging onto the nanotextured substrate located on a heater below. In the lower right corner the nanotextured substrate surface is shown. In the lower left corner, a concentric macroscopic wire coil used for comparison to mimic surface turbulizer effect is shown. The initial temperature of the substrate with nanofiber mat or a macroscopic wire coil was 120 °C.

In addition, the nanofiber mat creates turbulent eddies in the blown air, that is, the enhanced surface roughness due to nanofibers can act as a turbulizer and enhance heat transfer from the surface to an impinging air jet generated by a fan. To estimate this turbulization effect separately, that is, without the surface nanoroughness of the individual nanofibers, we used a concentric coil of a macroscopic wire shown in the inset in the lower left corner in Figure 8. This coil acted as a turbulizer generating turbulent eddies in the air jet. The turbulization effect of such a wire is more significant than that of the nanofibers, since the coiled wire perturbs the flow to a larger depth. It should be emphasized that turbulization of impinging jets by coils located at the surface can increase the local mass transfer (and similarly, the heat transfer) coefficient in the impinging jets up to 70% when the coils are located at radial distances $r < 2d_f$, with d_f being the jet diameter.[28] Our results discussed below show that the effect of nanofibers on the heat transfer coefficient extends well beyond a simple turbulizer due to their nanotexture. Note also that the effect of a coiled turbulizer is expected to be quite significant only in the case of the forced convection in the impinging jet, rather than in natural convection. Indeed, in the forced convection case the surface temperature reduction from 120 to 35.7 °C was observed, as indicated in Figure 9b with an asterisk. Note also that the surface temperature was reduced by forced convection to 37.6 °C in the case of the bare substrate without the concentric coil. Thus, the attachment of the concentric coil affected to some extent the turbulence in the impinging jet and was responsible for the additional surface temperature reduction of 1.9 °C. However, overall, this comparison shows that we deal here with cooling by a turbulent impinging air jet, since in the case of the natural convection, the surface temperature in the presence of coiled wire was reduced only from 120 to 116.9 °C, as indicated in Figure 9a with an asterisk.

3.4. Cooling in the Presence of Thorny Devil Nanofibers. The achieved steady-state surface temperature is plotted for the bare surface (0 min deposition time) and nanofiber-covered surfaces of different thicknesses (up to 30 min deposition time) for cooling under the conditions of natural convection in Figure 9a and forced convection in the impinging air jet in Figure 9b.

Figure 9a shows that natural convection can be responsible for the surface temperature reduction from 120 °C to no less than 103 °C only. In this case, the deepest cooling (down to 103 °C) is possible when the surface is covered with the finest solution-blown (with preheating) copper-plated nanofiber mat of the largest thickness (30 min deposition time), that is, with the surface possessing the largest surface area. The overall trend illustrated in Figure 9a is that a higher surface area results in a lower surface temperature, except the case of the thickest coating of electrospun nanofibers (the ES case). In the ES case, a too thick mat prevents air motion through it and acquires some insulating features.

Any further reduction of the surface temperature is possible only due to the forced convection. In this forced convection case, Figure 9b shows that a steady-state surface temperature could be reduced from 120 °C down to 32 °C. Once more, the finest solution-blown (with preheating) copper-plated nano-

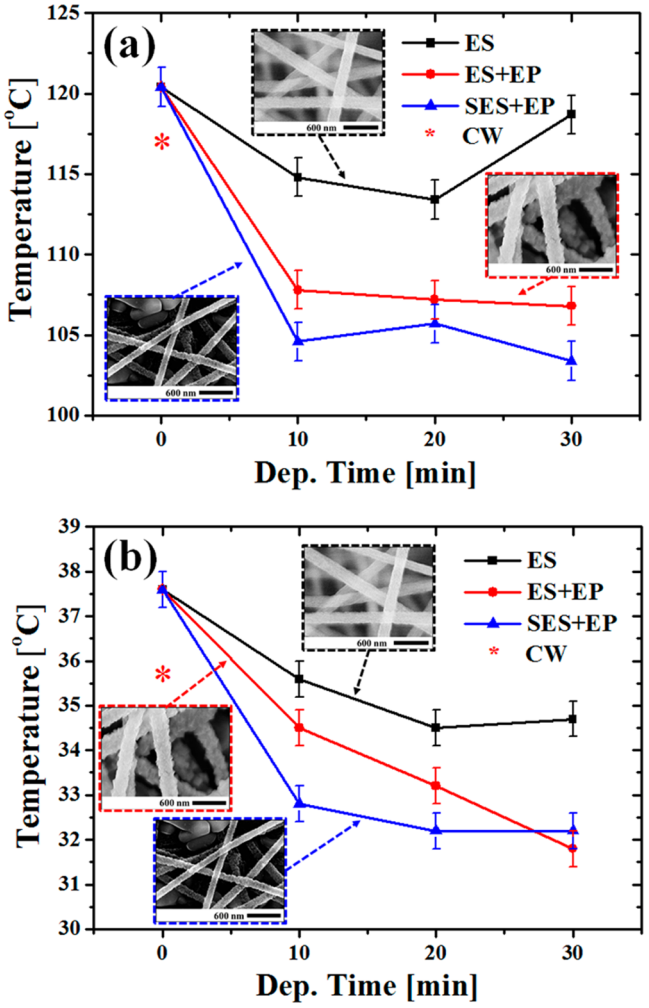

Figure 9. Surface temperature versus fiber-deposition time (determining the mat thickness) due to natural convection or an impinging air jet from a fan for different surfaces. The air temperature far from the surface is 19 °C (room temperature); the initial surface temperature in all the cases is 120 °C (the heater temperature). (a) Natural convection (no blowing). (b) Impinging jet (blowing). ES denotes purely electrospun nonplated polymer nanofibers; ES+EP denotes electrospun copper-plated thorny devil nanofibers; SES+EP denotes supersonically blown (formed with preheating at 500 °C) copper-plated nanofibers. The fiber deposition time varies from 0 min (bare substrate without nanofibers) to 30 min. The mat thickness increases with increasing in the nanofiber deposition time. Note that the asterisk symbol indicates temperature reduction due to air turbulization arising from the coiled wire.

fiber mats provide the highest heat removal rates and thus, the lowest surface temperatures (by several degrees Celsius) at all mat thicknesses, except the largest one corresponding to 30 min deposition time. In the latter case, the thickest mat of the finest nanofibers becomes less permeable for air flow, and a fluffier mat of electrospun copper-plated nanofibers slightly outperforms it. Except, the overall trend, once again, is that a higher surface area results in a lower surface temperature not only under conditions of the natural convection but also under forced convection. This is in agreement with the conclusion of ref 8, which was reached in the experiments with drop cooling.

Generally speaking, heat transfer from hot solid surfaces is associated with the surface area.[27] Therefore, the utmost enhanced cooling demonstrated by the supersonically blown nanofiber mats reveals their largest surface area. The results in Figure 6 imply that the characteristic pore size δ scales with the fiber diameter. Denote the number of pores in a unit volume of nanofiber mat as n. Thus, the mat porosity m can be evaluated as $m \sim \pi\delta^3 n/6$, while the surface area of the unit mat volume $S \sim \pi\delta^2 n = 6m/\delta$. This shows that the smaller is the pore size, or the fiber size, the larger is the surface area, and thus, the cooling effect of nanofibers on the heat removal rate and cooling. That explains why supersonically blown nanofibers revealed the utmost cooling effect.

3.5. Heat Tranfer Coefficient. Using the data in Figure 9, the effective heat transfer coefficient h_{eff} is defined as $h_{eff} = Q/[(T_s - T_\infty)A]$, where Q is the known power supply to the upper plane of the heater, $Q = 0.93$ W as described above, T_s is the steady-state surface temperature, T_∞ is the air temperature in the room, and A is the projected surface area of nanofibers, which is $A = 3 \times 3$ cm^2. The value of h_{eff} under different conditions are listed in Table 1. This Table shows that the presence of thorny devil nanofibers on the surface allows one to increase the heat transfer coefficient significantly in both natural and forced convection. Namely, the increase of about 20% in the natural convection, and about 41% in the forced convection above the values of h_{eff} corresponding to the surface with the coiled wire, is attributed to the effect of the thorny devil nanofibers alone, in particular, to their extension of the effective surface area.

Table 1. Heat Transfer Coefficient[a]

convection type	deposition time (min), t_{dep}		h_{eff} (W/m^2·K) ES	ES+EP	SES+EP
natural	coiled wire on the surface	10.6			
	0-bare surface	10.2			
	10		10.8	11.6	12.1
	20		10.9	11.7	11.9
	30		10.4	11.8	12.2
forced	coiled wire on the surface	61.9			
	0-bare surface	55.6			
	10		62.2	66.7	74.9
	20		66.7	72.8	78.3
	30		65.8	80.7	78.3

[a]The deposition time of $t_{dep} = 0$ refers to the bare surface case. For comparison, for the macroscopic concentric coil, the effective heat transfer coefficient $h_{eff} = 10.6$ and 61.9 W/m^2·K in the natural and forced convection cases, respectively. The following abbreviations are used: ES, EP, and SES refer to electrospun-only, electroplated, supersonically-electrospun, respectively.

4. THEORETICAL RESULTS AND COMPARISON WITH THE EXPERIMENT

A number of previous experimental and theoretical works dealt with cooling by impinging jets.[29−39] A number of empirical formulas for the Nusselt number Nu (the dimensionless heat transfer coefficient h) under different conditions were obtained, note in particular[29,30]

$$\mathrm{Nu} = 13\mathrm{Re}^{0.5}\frac{d_f}{H}, \quad \mathrm{Nu} = 1.16\mathrm{Re}^{0.447}\mathrm{Pr}^{0.33} \tag{1}$$

Here and hereinafter, $\mathrm{Nu} = hd_f/k$, with d_f being the issued jet diameter, k being the thermal conductivity, H being the

distance from the jet origin to the surface, $\mathrm{Re} = V_f d_f/\nu$ being the Reynolds number, with V_f and ν being the jet velocity at the origin and the kinematic viscosity, respectively, and Pr being the Prandtl number. The range of validity of these formulas is $H/d_f > 20$, and $H/d_f = 7-50$, respectively, which is significantly different from the experimental situation in the present work where $d_f/H = 2$, and thus, $H/d_f = 0.5$.

The need in the theoretical description of the heat transfer near the stagnation point of the impinging jets given the inapplicability of the empirical formulas or their disagreement with each other, was ascertained in refs 37 and 39, which revealed the following theoretical expressions for the Nusselt number, respectively

$$\mathrm{Nu} = 1.8\mathrm{Re}^{1/2}\mathrm{Pr}^{1/2}, \quad \mathrm{Nu} = 0.798\mathrm{Re}^{1/2}\mathrm{Pr}^{1/2}\left(\frac{d_f}{H}\right)^{1/2} \tag{2}$$

The second theoretical formula 2 revealed good agreement with the experimental data in ref 39 and is adopted and modified in the present work for the case of turbulent impinging jet used for cooling here, as described below. Consider the outer (main) part of the impinging jet of air from a fan toward a surface in the potential flow approximation assuming, as usual, that all viscous and convective heat transfer effects (molecular and turbulent) occur in the inner part of the flow-in the boundary layer near the surface and inside fluffy porous mats on it. The outer flow domain under consideration is sketched in Figure 10. In the present case, it is convenient

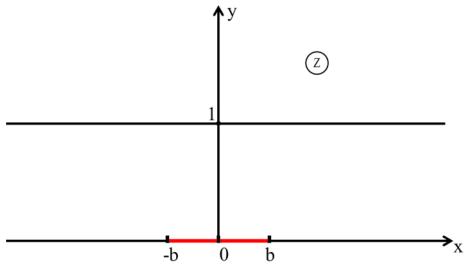

Figure 10. Sketch of an potential flow field of air in a jet issued at a fan $-b \le x \le b$, $y = 0$ and impinging onto a surface located at $-\infty \le x \le \infty$ and $y = 1$. The coordinates x and y, as well as b are rendered dimensionless by fan-to-surface distance H.

not to use directly the complex potential $\chi(z) = \varphi(x,y) + i\psi(x,y)$, where φ is the hydrodynamic potential, and ψ is the stream function, which are related, as usual, by the Cauchy–Riemann conditions. The complex potential is an analytical function of complex variable $z = x + iy$, with i being the imaginary unit. In the present case it is convenient to consider not $\chi(z)$ directly, but rather to use another analytic function of z associated with the conjugate velocity $\overline{V} = \mathrm{d}\chi/\mathrm{d}z$, namely

$$i\overline{V}(z) = v + iu \tag{3}$$

where u and v are the x- and y-velocity components, respectively.

In the impinging jet under consideration the real part of $i\overline{V}$ satisfies the following boundary conditions at the domain surfaces (cf. Figure 10), that is, at the fan level

$$v|_{y=0} = V_f \quad \text{for} \quad |x| \le b \tag{4}$$

$$v|_{y=0} = 0 \quad \text{for} \quad |x| > b \tag{5}$$

with V_f being the normal velocity in the y-direction produced by the fan, and at the impermeable wall (since the global outer problem considered here absorbs the boundary layer and the thin porous layer at the surface in this approximation)

$$v|_{y=1} = 0 \tag{6}$$

Then, the function $i\overline{V}(z)$ can be found from the boundary conditions for its real part at the surfaces using the Palatini formula which follows from the Schwartz formula for a disk.[40,41] Namely, this general solution thus obtained reads

$$i\overline{V}(z) = -\frac{i}{2}\int_{-\infty}^{\infty} v(\xi, y = 0)\coth\frac{\pi(\xi - z)}{2}\mathrm{d}\xi + \frac{i}{2}\int_{-\infty}^{\infty} v(\xi, y = 1)\tanh\frac{\pi(\xi - z)}{2}\mathrm{d}\xi \tag{7}$$

with ξ being a dummy (real) variable over the entire x-axis.

Substituting the boundary conditions eqs 4–6 and evaluating the integrals in eq 7 inside the domain shown in Figure 10, we obtain the following result

$$i\overline{V}(z) = V_f - \frac{iV_f}{\pi}\ln\left\{\frac{\sinh[\pi(b - z)/2]}{\sinh[\pi(b + z)/2]}\right\} \tag{8}$$

At the outer surface of the boundary layer near the surface as $y \to 1$, eq 8 yields the following velocity components

$$u = \gamma x, \quad v = \gamma(1 - y) \tag{9}$$

with

$$\gamma = V_f\tanh(\pi b/2) \tag{10}$$

It should be emphasized that in eqs 9 and 10 x, y, and b are rendered dimensionless by the distance from the fan to the surface H. In the present experiments the fan radius was 0.025 m and $H = 0.025$ m. So, the value of b is 1.

The heat transfer in the boundary layer of the impinging jet with the velocity field (eq 9) was calculated analytically in ref 39, and the corresponding Nusselt number is given by the second eq 2. Accordingly, the surface temperature T_s was related to the heat removal rate Q (equal to the heat supply rate in the steady-state situations considered here) as[39]

$$T_s = T_\infty + \frac{q}{0.798\mathrm{k}[V_f/(H\kappa)]^{1/2}} \tag{11}$$

Here, k and κ are the thermal conductivity and diffusivity of air, respectively.

It should be emphasized that ref 39 dealt with the impinging jets of the liquid eutectic alloys of gallium and indium (GaIn), and the molecular transport coefficients of GaIn were used in eq 11. In the present case, we are dealing with turbulent impinging jets of air. Therefore, the molecular transport coefficients k and κ should be replaced by the corresponding eddy ones k_T and κ_T, respectively. According to ref 42, turbulent eddy viscosity corresponding to the submerged axisymmetric jets $\nu_T = 0.015V_f d_f$, where $d_f = 2b$ (with b being dimensional), that is, the fan diameter. In the present case of a short impinging jet, another factor, 0.000028 is consistent with the experimental results for the surface temperature. Namely, $\nu_T = 0.000028V_f d_f$. On the other hand, according to ref 43, the turbulent Prandtl number in such jets $\mathrm{Pr}_T \approx 0.75$, and thus $\kappa_T = 0.000028V_f d_f/0.75$. Then, from eq 11 we obtain

$$T_s = T_\infty + q/\{0.798k[\tanh(\pi b/2)V_f/(H\kappa)]^{1/2} \times [0.000028V_f d_f/(0.75\kappa)]^{1/2}\} \quad (12)$$

where all transport coefficients are once again molecular (in the present case of air). This equation results in T_s= 31.8 °C, with b = 1, $q = Q/S$ = 1.03 kW/m^2, V_f = 10.2 m/s, H = 0.024 m, κ = 21.46 × 10^{-6} m^2/s, and d_f = 0.05 m, while the actual surface temperature was in the range of 32 °C < T_s < 38 °C in the forced convection case.

5. CONCLUSION

Supersonically blown below-74 nm nanofibers copper-plated to become the thorny-devil nanofibers, significantly enhance cooling of high temperature surfaces by impinging air jets or natural convection. In air cooling, such supersonically-blown and copper-plated nanofiber coatings at high-temperature surfaces outperform bare surfaces, surfaces with an additional turbulizer in the form of a coiled wire on the surface, as well as the surfaces with polymer electrospun nanofibers, or electrospun and copper-plated thorny devil nanofibers. In particular, surface coating consisting of ultrathin supersonically-blown copper-plated nanofibers allows one to reduce the surface temperature by the additional 5 °C in the case of the impinging air jet, and by 16 °C in the case of the natural convection. As a result, the heat transfer coefficient increases by about 41% in the forced convection, and about 20% in the natural one.

AUTHOR INFORMATION

Corresponding Authors

*Email: skyoon@korea.ac.kr.
*Email: ayarin@uic.edu.

Notes

The authors declare no competing financial interest.

ACKNOWLEDGMENTS

This work was supported by the Center for Inorganic Photovoltaic Materials (No. 2012-0001169) grant, NRF-2013R1A2A2A05005589, and 2011-0030433. This work was also supported by the Industrial Strategic Technology Development Program (10045221) funded by the Ministry of Knowledge Economy (MKE, Korea). A.L.Y. is grateful for the partial support of this work by NASA (Grant No. NNX13AQ77G).

REFERENCES

(1) Kim, S. Y.; Paek, J. W.; Kang, B. H. Thermal Performance of Aluminum-Foam Heat Sinks by Forced Air cooling. *IEEE Trans. Compon. Packag. Technol.* **2003**, *26*, 262−267.
(2) Darnell, J. R. Copper Heat Sinks for Electronic Devices and Method of Making Same. U.S. Patent No. 3,829,598, Aug 13, 1974.
(3) Kordas, K.; Tóth, G.; Moilanen, P.; Kumpumäki, M.; Vähäkangas, J.; Uusimäki, A.; Vajtai, R.; Ajayan, P. Chip Cooling with Integrated Carbon Nanotube Microfin Architectures. *Appl. Phys. Lett.* **2007**, *90*, 123105.
(4) Sayir, H.; Mehmet, A.; Cooper, E.; Icoz, T.; Schaepkens, M.; Liu, X. Advanced Heat Sinks and Thermal Spreaders. U.S. Patent Application No. 200070053168, Mar 8, 2007.
(5) Child, J. Conduction-Cooled CompactPCI Steers a Steady Course. *J. Mil. Electron. Comput.* **2009**, *11*, 46.
(6) Kinney, D. UAVs Embrace the Benefits of Direct Spray Cooling. *J. Mil. Electron. Comput.* **2009**, *11*, 22−25.
(7) Mudawar, I. Assessment of High-Heat-Flux Thermal Management Schemes. *IEEE Trans. Compon. Packag. Technol.* **2001**, *24*, 122−141.
(8) Sinha-Ray, S.; Zhang, Y.; Yarin, A. L. Thorny Devil Nanotextured Fibers: The Way to Cooling Rates on the Order of 1 kW/cm^2. *Langmuir* **2011**, *27*, 215−226.
(9) Jun, S.; Sinha-Ray, S.; Yarin, A. L. Pool Boiling on Nanotextured Surfaces. *Int. J. Heat Mass Transfer* **2013**, *62*, 99−111.
(10) Sinha-Ray, S.; Yarin, A. L. Drop Impact Cooling Enhancement on Nanotextured Surfaces. Part I: Theory and Results of the Ground (1*g*) Experiments. *Int. J. Heat Mass Transfer* **2014**, *70*, 1095−1106.
(11) Sinha-Ray, S.; Sinha-Ray, S.; Yarin, A. L.; Weickgenannt, C. M.; Emmert, J.; Tropea, C. Drop Impact Cooling Enhancement on Nanotextured Surfaces. Part II: Results of the Parabolic Flight Experiments [Zero Gravity (0g) and Supergravity (1.8 g)]. *Int. J. Heat Mass Transfer* **2014**, *70*, 1107−1114.
(12) Lembach, A.; Tan, H. B.; Roisman, I. V.; Gambaryan-Roisman, T.; Zhang, Y.; Tropea, C.; Yarin, A. L. Drop Impact, Spreading, Splashing, and Penetration in Electrospun Nanofiber Mats. *Langmuir* **2010**, *26*, 9516−9523.
(13) Weickgenannt, C. M.; Zhang, Y.; Lembach, A. N.; Roisman, I. V.; Gambaryan-Roisman, T.; Yarin, A. L.; Tropea, C. Nonisothermal Drop Impact and Evaporation on Polymer Nanofiber Mats. *Phys. Rev. E: Stat., Nonlinear, Soft Matter Phys.* **2011**, *83*, 036305.
(14) Weickgenannt, C. M.; Zhang, Y.; Sinha-Ray, S.; Roisman, I. V.; Gambaryan-Roisman, T.; Tropea, C.; Yarin, A. L. Inverse-Leidenfrost Phenomenon on Nanofiber Mats on Hot Surfaces. *Phys. Rev. E: Stat., Nonlinear, Soft Matter Phys.* **2011**, *84*, 036310.
(15) Medeiros, E. S.; Glenn, G. M.; Klamczynski, A. P.; Orts, W. J.; Mattoso, L. H. C. Solution Blow Spinning: A New Method to Produce Micro- and Nanofibers from Polymer Solutions. *J. Appl. Polym. Sci.* **2009**, *113*, 2322−2330.
(16) Sinha-Ray, S.; Yarin, A. L.; Pourdeyhimi, B. The Production of 100/400 nm Inner/Outer Diameter Carbon Tubes by Solution Blowing and Carbonization of Core−Shell Nanofibers. *Carbon* **2010**, *48*, 3575−3578.
(17) Sinha-Ray, S.; Zhang, Y.; Yarin, A. L.; Davis, S. C.; Pourdeyhimi, B. Solution Blowing of Soy Protein Fibers. *Biomacromolecules* **2011**, *12*, 2357−2363.
(18) Sinha-Ray, S.; Lee, M. W.; Sinha-Ray, S.; An, S.; Pourdeyhimi, B.; Yoon, S. S.; Yarin, A. L. Supersonic Nanoblowing: A New Ultra-Stiff Phase of Nylon 6 in 20−50 nm Confinement. *J. Mater. Chem. C* **2013**, *1*, 3491−3498.
(19) Liepmann, H.; Roshko, A. *Elements of Gasdynamics*; John Wiley & Sons: New York, 1957.
(20) Loitsyanskii, L. G. *Mechanics of Liquids and Gases*; Pergamon Press: Oxford, 1966.
(21) Courant, R.; Friedricks, K. O. *Supersonic Flows and Shock Waves*; Springer: Heidelberg, 1976.
(22) Kim, D. Y.; Sinha-Ray, S.; Park, J. J.; Lee, J. G.; Cha, Y. H.; Bae, S. H.; Ahn, J. H.; Jung, Y. C.; Kim, S. M.; Yarin, A. L.; Yoon, S. S. Self-Healing Reduced Graphene Oxide Films by Supersonic Kinetic Spraying. *Adv. Funct. Mater.* **2014**, DOI: 10.1002/adfm.201400732.
(23) Schlesinger, M.; Paunovic, M. *Electroplating*, 4th ed.; John Wiley & Sons: New York, 2000.
(24) Graham, A. K. *Electroplating Engineering Handbook*, 3rd ed.; VNR: New York, 1971.
(25) Park, J. J.; Lee, M. W.; Yoon, S. S.; Kim, H. Y.; James, S. C.; Heister, S. D.; Chandra, S.; Yoon, W. H.; Park, D. S.; Ryu, J. Supersonic Nozzle Flow Simulations for Particle Coating Applications: Effects of Shockwaves, Nozzle Geometry, Ambient Pressure, and Substrate Location upon Flow Characteristics. *J. Therm. Spray Technol.* **2011**, *20*, 514−522.
(26) Lee, M. W.; Park, J. J.; Kim, D. Y.; Yoon, S. S.; Kim, H. Y.; James, S. C.; Chandra, S.; Coyle, T. Numerical Studies on the Effects of Stagnation Pressure and Temperature on Supersonic Flow Characteristics in Cold Spray Applications. *J. Therm. Spray Technol.* **2011**, *20*, 1085−1097.
(27) Holman, J. *Heat Transfer*, 10th ed.; McGraw-Hill: Boston, 2010.

(28) Schlunder, E. U.; Gnielinski, V. Warme- und Stoffubertragung zwischen Gut und Aufprallenden Dusenstrahl. *Chem. Eng. Technol.* **1967**, *39*, 578−584.
(29) Gordon, R.; Cobonpue, J. Heat Transfer Between a Flat Plate and Jets of Air Impinging on It. In *International Developments in Heat Transfer*, Proceeding of the 2nd International Heat Transfer Conference, Boulder, CO, August 29-September 1, 1961.
(30) Livingood, J.; Hrycak, P. Impingement Heat Transfer from Turbulent Air Jets to Flat Plates-A Literature Survey. *NASA/TM* **1973**, *X-2778*, 1−23.
(31) Vallis, E. A.; Patrick, M. A.; Wragg, A. A. Radial Distribution of Convective Heat Transfer Coefficiet Between an Axysymmetric Turbulent Jet and a Flat Plate Held Normal to the Flow. In *Forced Convection*, Proceedings of the 6th International Heat Transfer Conference, Toronto, Canada, August 7−11, 1978.
(32) Hrycak, P. Heat Transfer from a Row of Jets Impinging on Concave Semi-Cylindrical Surface. In *Heat Transfer in Energy*, Proceedings of the 6th International Heat Transfer Conference, Toronto, Canada, August 7−11, 1978.
(33) Jeschar, R.; Potke, W. Modellversuche uber den Warmeubergang zwischen einen Isothermen Strahl und einer Ebenen Platte. *VDI-Ber.* **1970**, *N 146*, 129−136.
(34) Donaldson, C.; Snedeker, R.; Margolis, A. A Study of Free Jet Impingement Heat Transfer. Part 2. Free Jet Turbulent Structure and Impingement Heat Transfer. *J. Fluid Mech.* **1971**, *45*, 477−512.
(35) Dyban, E. P.; Mazur, A. I. *Convective Heat Transfer in Jet Impingement onto Blunt Bodies*; Naukova Dumka: Kiev, 1982.
(36) Liu, X.; Lienhard, J. H.; Lombara, J. S. Convective Heat Transfer by Impingement of Circular Liquid Jets. *J. Heat Transfer* **1991**, *113*, 571−582.
(37) Lienhard, J. H. Liquid Jet Impingement. *Annu. Rev. Heat Transfer* **1995**, *6*, 199−270.
(38) Silverman, I.; Nagler, A. High Heat Flux Cooling with Water Jet Impingement. In *Fundamental Research and Measurements*, Proceedings of ASME 2004 Heat Transfer/Fluids Engineering Summer Conference, Charlotte, NC, July 11−15, 2004.
(39) Silverman, I.; Yarin, A. L.; Reznik, S.; Arenshtam, A.; Kijet, D.; Nagler, A. High Heat-Flux Accelerator Targets: Cooling with Liquid Metal Jet Impingement. *Int. J. Heat Mass Transfer* **2006**, *49*, 2782−2792.
(40) Henrici, P. *Applied and Computational Complex Analysis*; Wiley: New York, 1974; Vol. *3*.
(41) Lavrent'ev, M.; Shabat, B. *Methods of the Theory of Functions of a Complex Variable*; Nauka: Moscow, 1973.
(42) Sinha-Ray, S.; Yarin, A. L.; Pourdeyhimi, B. Meltblowing: I. Basic Physical Mechanisms and Threadline Model. *J. Appl. Phys.* **2010**, *108*, 034912.
(43) Yarin, A. L. Self-similarity. In *Springer Handbook of Experimental Fluid Mechanics*; Tropea, C., Yarin, A. L., Foss, J. F., Eds.; Springer: Heidelberg, 2007.
(44) Reneker, D. H.; Yarin, A. L.; Fong, H.; Koombhongse, S. Bending Instability of Electrically Charged Liquid Jets of Polymer Solutions in Electrospinning. *J. Appl. Phys.* **2000**, *87*, 4531−4547.